Hollow laser self-confined plasma for extreme ultraviolet lithography and other applications

V. SIZYUK, A. HASSANEIN, AND T. SIZYUK

Argonne National Laboratory, Argonne, Illinois

Abstract

Laser-produced plasma (LPP) devices are being developed as a light source for the extreme ultraviolet (EUV) lithography applications. One concern of such devices is to increase the conversion efficiency of laser energy to EUV light. A new idea based on the initiation and confinement of cumulative plasma jet inside a hollow laser beam is developed and simulated. The integrated computer model (HEIGHTS) was used to simulate the plasma behavior and the EUV radiation output in the LPP devices. The model takes into account plasma heat conduction and magnetohydro-dynamic processes in a two-temperature approximation, as well as detailed photon radiation transport in 3D Monte Carlo model. The model employs cylindrical 2D version of a total variation-diminishing scheme (for the plasma hydrodynamics) and an implicit scheme with the sparse matrix linear solver (to describe heat conduction). Numerical simulations showed that the EUV efficiency of the proposed hollow-beam LPP device to be higher than the current standard devices.

Keywords: Extreme ultraviolet; Hollow laser; Laser plasmas; Plasma device modeling

1. INTRODUCTION

Since the invention of the transistor in 1947 and the integrated circuit (IC) in the late 1950s, semiconductor technology has undergone rapid advances. From a basic technical point of view, these developments have been straightforward. They have mainly involved putting more and smaller transistors on integrated circuits. More transistors allow for increased functionality, and smaller size allows for increased switching speed and less power consumption for each transistor. The whole process has conformed to Moore's law (Moore, 1965). Moore stated that the number of components per IC would roughly double every second year. In recent decades, the single most important driver of Moore's law has been the microlithography progress. The lithographic process generates a semiconductor wafer partially covered with photoresist, so that the uncovered regions are available for different kinds of processing, such as etching, ion implantation, or metallization. One of the most important lithographic processes is exposure, when light shines on selected parts of the resist and forms future microelectronic elements (Levinson, 2001). Resolution of an optical system,

such as a projection–lithography system, is traditionally determined by the Rayleigh criterion (*resolution* $= 0.61$ λ/NA, with wavelength λ of used light, and numerical aperture NA of used optical system). Because increasing the numerical aperture has a definite limit, utilizing the smallest wavelength for projection–lithography is the path to progress in semiconductor technology. Use of extreme ultraviolet light (EUV, where the wavelength is between 10 and 15 nm) is the most advanced method today (Attwood, 2004).

EUV light is absorbed strongly in most materials, including gases; thus, all optics and the source should be placed into a vacuum. For the same reason, lenses cannot be used: optical systems should consist of mirrors. Because the reflection of a single surface is very low (about 4%), stacked multilayers, of which the reflection adds up, are used or bent crystals which extend the diagnostic application into the X-ray regime (Dunn *et al.*, 2005; Labate *et al.*, 2004). The EUV light can be generated by several methods: discharge produced plasma (DPP) (Wagner *et al.*, 1996), laser produced plasma (LPP) (Fiedorowicz, 2005), or synchrotron radiation (Dattoli *et al.*, 2005; Ozaki *et al.*, 2006). Each method has its advantages and disadvantages. To meet the requirements of the Intel Lithography Roadmap goals for high-volume manufacturing (Silverman, 2002) and International SEMATECH's EUV Source Program goal (Bakshi,

2006), the EUV source is required to have a power of more than 120 W at a wavelength of 13.5 nm (2% bandwidth). Various LPP and DPP devices are being investigated by different research groups (Stamm, 2004*b*; Pankert *et al.*, 2005; Krücken *et al.*, 2004). At present, several of the EUV sources come close to the power level demanded by commercial chip manufacturers. The efficiency of generating EUV radiation is the key factor in successful development of the source (Ullrich *et al.*, 1987; Faenov *et al.*, 2004). Many additional factors are related to the EUV device efficiency, including plasma material, form and size of the radiated area, collectable solid angle, and debris amount. Because many physical processes are involved, and many technical problems need to be solved when optimizing a particular EUV device, laboratory experiments would be very expensive and may be impossible; therefore, only computer modeling can generate a complete picture of EUV devices within a reasonable time and at a reasonable cost.

Ideally, an integrated physical model should be developed specifically for simulating plasma behavior in both DPP and LPP devices. The model should include atomic physics, hydrodynamics, plasma heat conduction, and photon radiation transport. The EUV source should be modeled completely: from the energy input mechanism and plasma formation, up to EUV output from the pinch or laser target and the mirror collector system. Each physical process should be described adequately, and each physical problem should be solved using the most advanced numerical scheme to enhance accuracy and to reduce computational time. The radiation conditions at the intermediate focus of a manufacturers EUVL stepper can then be predicted most accurately.

This paper is organized as follows. First, we present the integrated model, implemented in computer package, for simulating LPP devices for EUV lithography. The model is based on previous progress in simulation of discharge- and laser-produced plasma devices of our high energy interaction with general heterogeneous target systems (HEIGHTS) package (Hassanein *et al.*, 2003, 2004*a*, 2004*b*; Miloshevsky *et al.*, 2006). We describe general model components and system equations, application of equations to LPP device simulation, numerical methods used, and benchmarking of results. Next, we discuss the influence of a generated magnetic field. We then present simulation results derived from our theoretical model. Based on these results, we propose the use of a novel plasma confinement concept to increase EUV throughput and overall LPP device efficiency.

2. MATHEMATICAL MODEL

2.1. Governing equations

To construct a comprehensive and efficient integrated model, we solved plasma formation and motion using a set of four conservation laws: mass, momentum, energy, and magnetic field (we use Gaussian units unless indicated otherwise). The conservation law of a parameter q can be given in differential form as:

$$\frac{\partial q}{\partial t} + \nabla \cdot \mathbf{F}_q = 0 \tag{1}$$

where $\mathbf{F}_q$ is flux of this parameter. By considering plasma matter as a continuous, compressible medium, we expanded Eq. (1), and obtained the following expressions for conservation of mass, momentum, and total energy:

$$\frac{\partial \rho}{\partial t} + \nabla \cdot (\rho \mathbf{v}) = 0$$

$$\frac{\partial}{\partial t} \rho \mathbf{v} + \nabla \cdot (\rho \mathbf{v}\mathbf{v} + p_h) = 0.$$

$$\frac{\partial e_h}{\partial t} + \nabla \cdot [\mathbf{v}(e_h + p_h)] = 0 \tag{2}$$

Here, ρ is the density of plasma; $\mathbf{v}$ is the velocity of plasma; p_h is the hydrodynamic pressure; and $e_h = (\rho v^2/2) + e_{\text{int}}$ is the sum of kinetic and internal energy densities of plasma.

Laboratory plasma experiments typically include the influence of an external electromagnetic source. The electric current can also be generated by the intensive heating of a local plasma area. A general magnetohydrodynamic (MHD) model should consider this electric current $\mathbf{j}$ as the source of the magnetic field in the plasma. The induced magnetic field $\mathbf{B}$ is the source of forces that disturb the initial plasma. A self-consistent process was incorporated into the hydrodynamic equation set, Eq. (2), as external force $\mathbf{F}_{ex}$:

$$\frac{\partial \rho}{\partial t} + \nabla \cdot (\rho \mathbf{v}) = 0.$$

$$\frac{\partial}{\partial t} \rho \mathbf{v} + \nabla \cdot (\rho \mathbf{v}\mathbf{v} + p_h) = \mathbf{F}_{ex}.$$

$$\frac{\partial e_h}{\partial t} + \nabla \cdot [\mathbf{v}(e_h + p_h)] = \mathbf{v} \cdot \mathbf{F}_{ex}. \tag{3}$$

We used the sum of the Lorenz and electrical forces $\mathbf{E} = -(1/c)\mathbf{v} \times \mathbf{B} + \eta \mathbf{j}$ that act on the unit charge (electric field strength) as the external force $\mathbf{F}_{ex}$. Also, we introduced heat conduction, radiation transport, and magnetic diffusion terms into Eq. (3). The MHD set is considered for the two-temperature approximation model; that is, the ion part is separated in the total energy equation. After correction of the magnetic field divergence (Tóth, 2000; Tóth & Odstrčil, 1996), the most general form of the MHD equation set was obtained and implemented for the HEIGHTS model. The following MHD equations thus form the basic of our calculations:

$$\frac{\partial \rho}{\partial t} + \nabla \cdot (\rho \mathbf{v}) = 0$$

$$\frac{\partial \rho \mathbf{v}}{\partial t} + \nabla \cdot \left(\rho \mathbf{v}\mathbf{v} + p_{tot} - \frac{\mathbf{B}\mathbf{B}}{4\pi\mu}\right) = -\frac{1}{4\pi\mu}\mathbf{B}(\nabla \cdot \mathbf{B})$$

$$\frac{\partial e_{tot}}{\partial t} + \nabla \cdot \left[\mathbf{v}(e_{tot} + p_{tot}) - \frac{1}{4\pi\mu}(\mathbf{v}\cdot\mathbf{B})\cdot\mathbf{B} \right.$$

$$\left. + \frac{c^2\eta}{16\pi^2\mu^2}(\nabla\times\mathbf{B})\times\mathbf{B} - \lambda_e\nabla T_e - \lambda_i\nabla T_i - \mathbf{S}_{rad} \right]$$

$$= Q_{las} - \frac{1}{4\pi\mu}(\mathbf{v}\cdot\mathbf{B})\cdot(\nabla\cdot\mathbf{B}).$$

$$\frac{\partial e_i}{\partial t} + \nabla\cdot[\mathbf{v}(e_i + p_i) - \lambda_i\nabla T_i] = 3\frac{m_e n_e}{m_i \tau_e}(k_B T_e - k_B T_i)$$

$$\frac{\partial\mathbf{B}}{\partial t} + \nabla\cdot(\mathbf{v}\mathbf{B} - \mathbf{B}\mathbf{v}) + \frac{c^2}{4\pi\mu}\nabla\times(\eta\nabla\times\mathbf{B}) + \frac{ck_B}{en_e}\nabla n_e\times\nabla T_e$$

$$= -\mathbf{v}(\nabla\cdot\mathbf{B}). \quad (4)$$

Here, e_{tot} is the total energy, which includes the hydrodynamic part, $e_h = e_e + e_i + e_{kin}$, and the magnetic part $e_m = (B^2/8\pi\mu)$; e_e is the electronic component of the plasma energy, which includes thermal energy of electron and ionization energy; e_i is the ion component of the plasma energy; and $e_{kin} = (\rho v^2/2)$ is the kinetic energy of the plasma. Analogous to energy, pressure has hydrodynamic and magnetic parts: $p_{tot} = p_e + p_i + (B^2/8\pi\mu)$. We use the subscript e for electrons and i for ions. Magnetic diffusion processes are taken into account as the Joule heat term, $(c^2\eta/16\pi^2\mu^2)(\nabla\times\mathbf{B})\times\mathbf{B}$, in the total energy equation and as the diffusion term, $(c^2/4\pi\mu)\nabla\times(\eta\nabla\times\mathbf{B})$, in the magnetic field equation, where η is resistivity and μ is magnetic permeability. In the calculations below, we assume $\mu = 1$ for the plasma. The thermal conduction in the plasma is considered as the combined result of the electron $\lambda_e\nabla T_e$ and ion $\lambda_i\nabla T_i$ conductivity, where λ is the conductivity coefficient and T is the temperature. The radiation transport process is represented here as flux $\mathbf{S}_{rad}$ and the laser heating source as Q_{las}. Also taken into account is the energy interchange between electrons and ions in the form $3(m_e n_e/m_i\tau_e)(k_B T_e - k_B T_i)$ (Braginskii, 1965) and the thermally generated magnetic field $(ck_B/en_e)\nabla n_e\times\nabla T_e$ (Goldman & Schmalz, 1987; Mora, 1981). Here m is the mass; n_e and τ_e are electron concentration and the relaxation time; c is the speed of light; e is the electron charge; and k_B is the Boltzmann constant.

2.2. Application

Eq. (4) constitutes the initial equation set used by the HEIGHTS package generally for modeling plasma processes. The conditions of a particular problem lead to the modification of the main equations. Modern LPP devices for EUVL work in the laser radiation intensity range of 10^{10}–10^{11} W/cm^2 (Harilal *et al.*, 2005; Myers *et al.*, 2005; Richardson *et al.*, 2004*b*; Keyser *et al.*, 2003). Self-generated magnetic fields in laser-produced plasmas are of much theoretical and exper-

imental interest because of their role in the laser plasma dynamics, and as a result, are important in the macroscopic plasma parameters (temperature, density, and EUV output) (Widner, 1973; Colombant & Winsor, 1977; Mora, 1981; Thareja & Sharma, 2006). Interest in this area is due to transport characteristics, such as thermal transport, lateral plasma flow, and fast plasma blowoff that affect the performance of the target. These characteristics are, in turn, related to the properties of large-scale magnetic fields generated in the system. The self-generated magnetic field holds an important place in the modeling of inertial confinement fusion processes, where laser irradiation reaches $\sim 10^{16}$ W/cm^2 (Nakamura *et al.*, 2006; Desai & Pant, 2000). We carried out numerical experiments to study the influence of the thermally generated magnetic field on the plasma parameters and the EUV output in the lithography energy range (Sizyuk *et al.*, 2006). Simulations of the LPP device with droplet and planar targets showed a very small dependence of the plasma parameters from the thermomagnetic source for the radiation power density of 10^{10}–10^{11} W/cm^2. We were thus able to omit the magnetic source and magnetic field in Eq. (4), and reconstruct the initial equations for more efficient calculations for this EUVL work.

Because the plasma device and plasma motion processes have cylindrical symmetry, we formulated Eq. (4) set in cylindrical coordinates system and integrated the obtained expressions for the azimuth angle φ. Since the final transformed equations had convective terms (hydrodynamic flux) and dissipative terms (heat conduction, laser heating, radiation transport, and electron–ion interaction), we used splitting of the physical processes in our numerical algorithm to separate the hyperbolic and parabolic parts (Miloshevsky *et al.*, 2006; Sizyuk *et al.*, 2006; Kovenya *et al.*, 1988; Leveque, 2002). The general solution has two stages: convective and dissipative. The transformed initial equation set is given in matrix form as

$$\frac{\partial\mathbf{U}}{\partial t} + \frac{1}{r}\frac{\partial}{\partial r}[r\mathbf{F}(\mathbf{U})] + \frac{\partial\mathbf{P}(\mathbf{U})}{\partial r} + \frac{\partial\mathbf{G}(\mathbf{U})}{\partial z} = \mathbf{\Omega}, \quad (5)$$

where the hydrodynamic fluxes are

$$\mathbf{U} = \begin{bmatrix} \rho \\ \rho v^r \\ \rho v^z \\ e_h \\ e_i \end{bmatrix} \quad \mathbf{F}(\mathbf{U}) = \begin{bmatrix} \rho v^r \\ \rho v^r v^r \\ \rho v^z v^r \\ v^r(e_h + p_h) \\ v^r(e_i + p_i) \end{bmatrix}$$

$$\mathbf{P}(\mathbf{U}) = \begin{bmatrix} 0 \\ p_h \\ 0 \\ 0 \\ 0 \end{bmatrix} \quad \mathbf{G}(\mathbf{U}) = \begin{bmatrix} \rho v^z \\ \rho v^r v^z \\ \rho v^z v^z + p_h \\ v^z(e_h + p_h) \\ v^z(e_i + p_i) \end{bmatrix}, \quad (6)$$

and the dissipative terms are combined in the source $\mathbf{\Omega}$

$$\mathbf{\Omega} = \begin{bmatrix} 0 \\ 0 \\ 0 \\ Q_{e,th} + Q_{i,th} + Q_{las} + Q_{rad} \\ Q_{i,th} + Q_{ei} \end{bmatrix}. \tag{7}$$

Here $Q_{e,th}$ is the electron heat conduction, $Q_{i,th}$ is the ion heat conduction, Q_{rad} is the radiation transport, and Q_{ei} is the electron-ion interaction. The conservative form of the initial equations allows the use of the TVD method in the Lax–Friedrich formulation (TVD–LF) (Tóth & Odstrčil, 1996; Leveque, 2002) for solution of the convective stage given by Eq. (5). The numerical scheme for the TVD–LF method applied to the cylindrical symmetry case is presented in Hassanein *et al.* (2004*a*). Following the splitting method, the *Q*-terms in Eq. (7) are calculated separately with the second (dissipative) stage of the HEIGHTS solver and are used as correctors of the main TVD-LF solution. An implicit numerical scheme with sparse matrix linear solvers is used for calculating the terms $Q_{e,th}$ and $Q_{i,th}$ (Miloshevsky *et al.*, 2006; Sizyuk *et al.*, 2006). The electron–ion interaction term $Q_{ei} = 3(m_e n_e/m_i \tau_e)(k_B T_e - k_B T_i)$ is calculated for each hydrodynamic step and used as input in the right side of Eq. (7).

The Monte Carlo method is used for modeling the LPP radiation processes: laser heating, photon radiation transport in the plasma, and the EUV output. With regard to LPP radiation transport, radiation fluxes should be determined to solve two main problems: (1) correction of the plasma thermal energy and, as a result, correction of the plasma motion in the device, and (2) determination of the final useful part of the radiation flux (i.e., EUV output). These problems determine the different requirements for the flux data and the numerical techniques needed to solve the photon transport problem. Correct calculation of the energy-space redistribution in full spectrum of the plasma plays an important role in solving the first problem. The constructed model describes radiation transport adequately only if it takes into account the optical thickness of the plasma in a large number of spectral groups. The full spectrum of the LPP plasma is divided into narrow spectral groups with separation of the strongest lines. The total number of the spectral groups was optimized to accurately describe the radiation energy redistribution for a reasonable computational power. As previous calculations show (Morozov *et al.*, 2004*a*), the MHD results have an acceptable error for total spectral groups of about 10^3. However, such number of groups is unacceptable for investigations in the EUV band of interest, 2% at 13.5 nm. For this reason, we use two sets of optical opacities: general (for full-energy redistribution calculations) and specific (for calculations in the interesting spectral band). The main hydrodynamic simulations use

general opacity tables and calculate the evolution of the plasma temperature and density. The final EUV simulations use the detailed opacities to estimate the LPP device efficiency.

The Monte Carlo algorithm of radiation transport models three elementary processes: the emission, motion, and absorption of separate photons (Fig. 1). This approach has the advantage of considering complex geometries within the computational domain. The radiation transport model is three-dimensional (3D); that is, the photon motion is considered in a 3D Cartesian coordinate system. The cylindrical case involves the accumulation of statistical events in the two-dimensional (2D) system of the LPP device. Figure 1 schematically shows the trajectory of an individual photon in the two coordinate systems.

Studying the trajectory, as well as the number of emitted and absorbed energy at each point of the plasma domain (or the points of major interest); one can calculate the redistribution of energy due to photon transport. Because simulation of all photons in the domain is problematic (computation power is limited), each energy portion is assumed to be a monochromatic set of photons. Hence, a macro-photon has the properties (absorption and emission probabilities) of the component photons, and the energy is equal to the sum of the energies of all photons in the set. To optimize the algorithm and decrease computation time, we introduced a system of weight factors into the Monte Carlo radiation transport model. Two major weight factors were allocated: normalization of the emitted macro-photon relative to the most radiated cell of the computational domain and normalization relative to the optical thickness of cell. The first
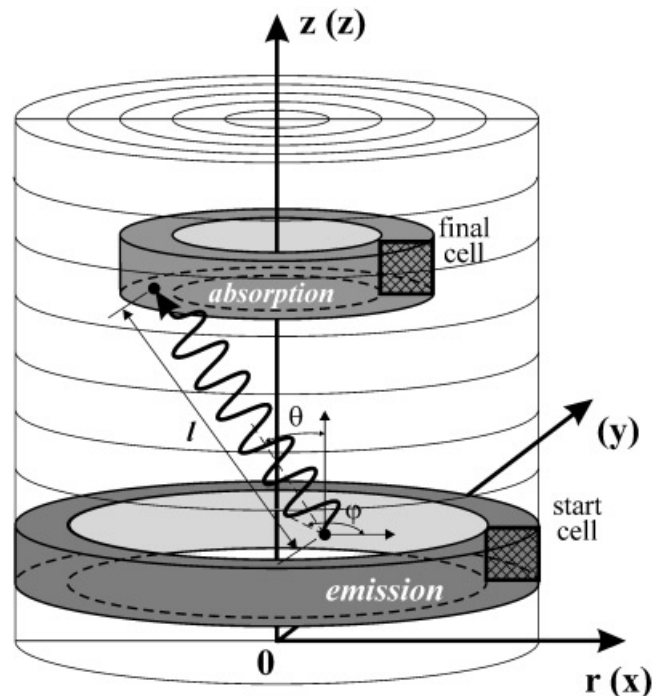

Fig. 1. Simulation of photon emission, transport, and absorption in two coordinate systems: 2D (r, z) and 3D (x, y, z).

weight factor is obtained from the emission process analysis and accelerated calculations due to the neglect of the emission of cold cells. Because of the second weight factor, so-called idle processes are ignored, namely, situations involving the emission and the absorption of the photon in the same cell (absorbed lines). A third weight factor can be useful for a strongly nonuniform mesh. The volume of the emitting cell can be so small that the amount needed for simulating photon bundles will not be sufficient to obtain accurate results. The volume weight coefficient should increase the computation accuracy in this case.

As reported by Zeldovich and Raizer (1966), the emission coefficient k_{em} should be integrated with Planck's function $B(\omega)$ in the full spectrum to obtain number N of emitted photons in the space (from a unit volume in a unit time):

$$N = 4\pi \int_0^\infty \frac{k_{em}B(\omega)}{\hbar\omega} \, d\omega. \tag{8}$$

$$B(\omega) = \frac{\hbar\omega^3}{4\pi^3c^2} \left[\exp\left(\frac{\hbar\omega}{T}\right) - 1 \right]^{-1}. \tag{9}$$

The following expression is derived after substituting Eq. (9) into (8)

$$N = \int_{E_{\min}}^{E_{\max}} \frac{k_{em}(E,T,\rho)E^2}{\hbar^3\pi^2c^2} \left[\exp\left(\frac{E}{T}\right) - 1 \right]^{-1} dE \quad (\text{cm}^{-3}\,\text{s}^{-1}), \tag{10}$$

where E is the energy of emitted photon (eV); $E_{\min}, E_{\max}$ are the spectral energy range (eV); $k_{em}(E,T,\rho)$ is the emission coefficient (cm^{-1}); T is the plasma temperature (eV); ρ is the plasma density (g/cm^3); $\hbar$ is Planck's constant (eV·s); and c is the speed of light (cm/s).

The total number of photons emitted in a separate cell (i,j) of the computation domain in unit time is

$$N_{i,j} = V_{i,j} \int_{E_{\min}}^{E_{\max}} \frac{k_{em}(E,T_{i,j},\rho_{i,j})E^2}{\hbar^3\pi^2c^2} \left[\exp\left(\frac{E}{T_{i,j}}\right) - 1 \right]^{-1} dE, \tag{11}$$

where $V_{i,j}$ is the volume of the cell (i,j). For calculating Eq. (11), the HEIGHTS package used Simpson's integration method. One of the key parts of the developed Monte Carlo algorithm is evaluation of the most radiated cell. An incorrect choice of the cell with maximum photons results in a shift of the weight coefficient and a slump in the calculation efficiency. We used the criterion $F_L = \rho^2 T^4 V_{cell}$ in our developed numerical algorithm for the first step. Because this simple function does not always give correct results, subsequent calculations used information about the photon emission that was obtained in the previous time step. This technique gives a significant increase in calculation efficiency. The total sum of photons in the most radiated cell is normalized to the initial amount of the macro-photons.

Based on this assumption, the first weight coefficient of the macro-photon is

$$W_1 = \frac{N^{\max}}{N_{sim}}. \tag{12}$$

The limits imposed by a reasonable degree of accuracy and the available computational capabilities determine the total sum of the macro-photons N_{sim} used to simulate the emission from the most radiated cell. The physical number of photons in the most radiated cell $N^{\max}$ is calculated from Eq. (11). To obtain acceptable accuracy in the radiation transport calculations, we used N_{sim} of about 10^3. A typical situation for the LPP modeling is the case when any spectral band is mostly absorbed within a volume of one cell. In this case, the Monte Carlo algorithm goes to the "idle" cycles. The macro-photon energy is subtracted from the initial cell energy at the emission stage and is added at the absorption stage in the same cell. A second weight factor is introduced to avoid this problem:

$$W_{2\{i,j\}}^n = k_{abs}(E_n, T_{i,j}, \rho_{i,j})\Delta r_i, \tag{13}$$

where $W_{2\{i,j,k\}}^n$ is the weight factor of nth spectral band in the cell (i,j); $k_{abs}(E_n, T_{i,j}, \rho_{i,j})$ is the absorption coefficient of nth spectral range in the cell (i,j); and Δr_i is the characteristic size of the cell. In the case of Eq. (13) less than 1, the second weight factor is assumed to be equivalent to 1. In that way, the developed algorithm avoids simulation of the absorbed lines. The photon emission simulation for the cell (i,j) is derived as follows:

(1) Calculation of the total sum of emitted photons in the most radiated cell by integration within each spectral group:

$$N^{\max} = \frac{V^{\max}}{\hbar^3\pi^2c^3} \sum_{n=1}^M k_{em}(E_n, T^{\max}, \rho^{\max})$$

$$\times \int_{E_n}^{E_{n+1}} E^2 \left[\exp\left(\frac{E}{T^{\max}}\right) - 1 \right]^{-1} dE. \tag{14}$$

The emission coefficient $k_{em}(E_n, T^{\max}, \rho^{\max})$ is assumed to be constant within one spectral group; and M is the total number of groups.

(2) Calculation of the first weight coefficient W_1 from Eq. (12).

(3) Simulation of the emitted photon distribution by the spectral groups

$$N_{i,j}^n = \frac{V_{i,j}k_{em}(E_n, T_{i,j}, \rho_{i,j})}{\hbar^3\pi^2c^2} \int_{E_n}^{E_{n+1}} E^2 \left[\exp\left(\frac{E}{T_{i,j}}\right) - 1 \right]^{-1} dE. \tag{15}$$

(4) Calculation of $W_{2\{i,j\}}^n$ by Eq. (13).

(5) Computation of the total sum of the macro-photons, which is used for emission modeling in the cell (i, j):

$$N_{i,j}^{sim} = \frac{1}{W} \sum_{n=1}^{M} \frac{N_{i,j}^n}{W_{2\{i,j\}}^n}.$$ (16)

(6) Normalization of the emission spectrum for future sampling of photon energy:

$$P_n = \frac{N_{i,j}^n}{W_1 W_{2\{i,j\}}^n N_{i,j}^{sim}},$$

i.e.,

$$\sum_{n=1}^{M} P_n = 1.$$ (17)

Photon energies are assumed to be distributed in an equiprobable manner within one spectral group. Linear interpolation is used for sampling the emitted particle energy E_{ph}. By taking into account the weight factors, the energy of the emitted macro-photon $E_{ph}^{sim} = E_{ph} W_1 W_{2\{i,j\}}^n$ is calculated as a function of spectral group number n. The group number is determined from the real physical energy of photon E_{ph}. The value of E_{ph}^{sim} should be subtracted from the cell energy by the emission simulation and added by the absorption process.

The starting position and direction of the macro-photon inside the cell are modeled as equiprobable events. The curvature of space is taken into consideration along the r-axis in the case of cylindrical symmetry. Final expressions for the macro-photon start position in the (r, z) coordinate system are given by

$$z = z_1 + \xi(z_2 - z_1),$$ (18)

$$r = \sqrt{r_1^2 + \xi(r_2^2 - r_1^2)},$$ (19)

where r_1 and r_2 are the cell borders along the r-axis; z_1 and z_2 are the cell borders along the z-axis; and ξ is a random number within the interval $[0, 1]$.

Attenuation of the light intensity due to matter absorption is described by the expression $I = I_0 \exp[-\int_0^l k_{abs}(\omega, l)\, dl]$ (Siegel & Howell, 1981), or in photon number terms,

$$N(\omega) = N_0(\omega) \exp\left[-\int_0^l k_{abs}(\omega, l)\, dl\right],$$ (20)

where $N_0(\omega)$ is the initial number of photons with frequency ω, and l is the path length in matter. By considering the photon path within one cell (where the absorption coefficient is independent of coordinates), one can express attenuation as

$$N(\omega) = N_0(\omega) \exp[-k_{abs}(\omega)l].$$ (21)

Consequently, the absorption or the transition probability of a photon on the path length l in cell (i, j) is

$$P_{i,j}^{abs}(\omega) = 1 - \frac{N(\omega)}{N_0(\omega)} = 1 - \exp[-k_{abs\{i,j\}}(\omega)l],$$ (22)

$$P_{i,j}^{trans}(\omega) = \exp[-k_{abs\{i,j\}}(\omega)l].$$ (23)

To complete simulation of the absorption process in the plasma, we use the absorption coefficient (which depends on matter parameters in the computational domain cell and on photon energy) and the photon path length in this cell.

The laser beam is modeled as a directional flux of the macro-photons in analogy to the above Monte Carlo theory. The separate macro-photon has the same properties (absorption, reflection probability, etc.) as the real laser radiation photon. The total sum of real photons W_{macro} in one macro-photon is estimated from the required accuracy and available computational power:

$$N_{macro} = \frac{N_{real}}{W_{macro}}, \quad N_{real} = \frac{P_{las}}{E_{ph}}.$$ (24)

Here, P_{las} is the momentary laser power and E_{ph} is the energy of a real laser radiation photon. The inverse bremsstrahlung is assumed to be the main process by which the laser radiation was absorbed by the plasma electrons. The classical value for the absorption coefficient k_{abs}^{las} that defines this collisional absorption mechanism is given (Johnston & Dawson, 1973) by

$$k_{abs}^{las} = \frac{16\pi Z n_e^2 e^6 \ln \Lambda(\nu)}{3c\nu^2 (2\pi m_e k_B T_e)^{3/2} (1 - \nu_p^2/\nu^2)^{1/2}}.$$ (25)

where again e, n_e, m_e, T_e are the electron charge, density, mass, and temperature, respectively; Z is the normalized ionic charge; ν is the frequency of laser light; $\nu_p = \sqrt{(n_e e^2/\pi m_e)}$ is the plasma frequency; and k_B is the Boltzmann constant. The Coulomb logarithm (Spitzer, 1962) is given by

$$\ln \Lambda = \ln\left[\frac{3}{2}\sqrt{\frac{(k_B T_e)^3}{\pi n_e}}\frac{1}{Ze^3}\right].$$ (26)

The condition $\nu_p \geq \nu$ in any space point is used to simulate the photon reflection. The modeling mechanism of the laser heat as well as the EUV radiation output is analogous to the radiation transport, excluding the sampling of the start position and direction of the macro-photon. These parameters are determined from the experimental laser beam direction and geometry.

2.3. Validation and benchmarking

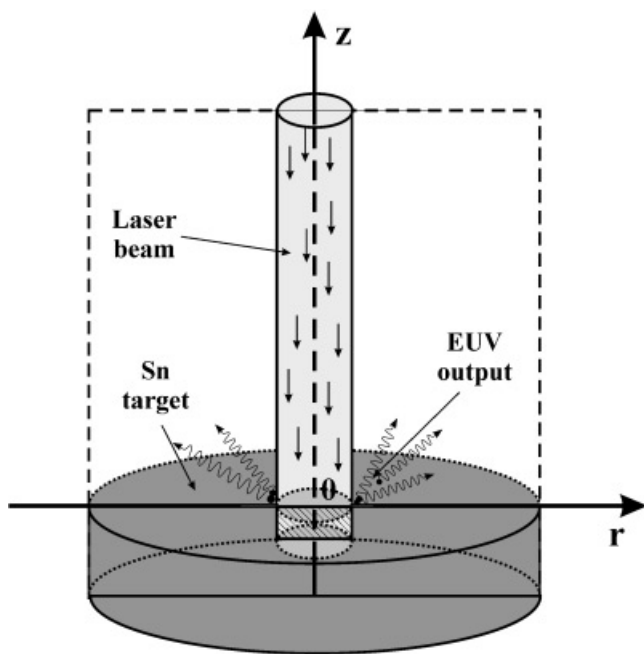To validate the model and benchmark the code, we solved several test problems and compared our results with known

Fig. 2. Schematic illustration of laser-target interaction in LPP devices.

Fig. 3. Comparison of HEIGHTS calculations with published experimental and theoretical data.

analytical and experimental results. The calculation blocks (TVD–LF, thermal conductivity, radiation transport, etc.) were tested separately and in various combinations (Hassanein *et al.*, 2003, 2004*a*, 2004*b*; Miloshevsky *et al.*, 2006; Sizyuk *et al.*, 2006; Sizyuk & Hassanein, 2002; Morozov *et al.*, 2004*a*). Here, we present the final benchmarking applicable to the EUV lithography problem. The EUV output from an LPP device with planar geometry of the tin target was calculated, and the results were compared with the experimental and theoretical data (Spitzer *et al.*, 1996). The geometrical arrangement of the simulation is shown schematically in Figure 2. The device modeled with the HEIGHTS package had an Nd:YAG laser, delivering 0.3 J at 1.064-μm wavelength in a 7.5-ns pulse. The laser radiation intensity was controlled by tuning of the laser spot radius. The minimum spot size at the target was about 20 μm.

The physical and mathematical model developed for this problem included all the above-discussed computational blocks: TVD–LF scheme for hydrodynamic, implicit sparse matrix solution for parabolic terms, Monte Carlo radiation transport, Monte Carlo laser absorption, and Monte Carlo model of EUV output. This assembled model was tested in 2D and 3D numerical schemes, which gave close results. It was also tested with several versions of spatial meshes (2D: 100 × 250 cells with minimal size of cell in the region of interest ~1 μm and 65 × 110 cells with size ~5 μm). A final parameter that served as a criterion for benchmark evaluation was the total EUV output into 2π sr solid angle, i.e., the conversion efficiency (CE) of the LPP device given by:
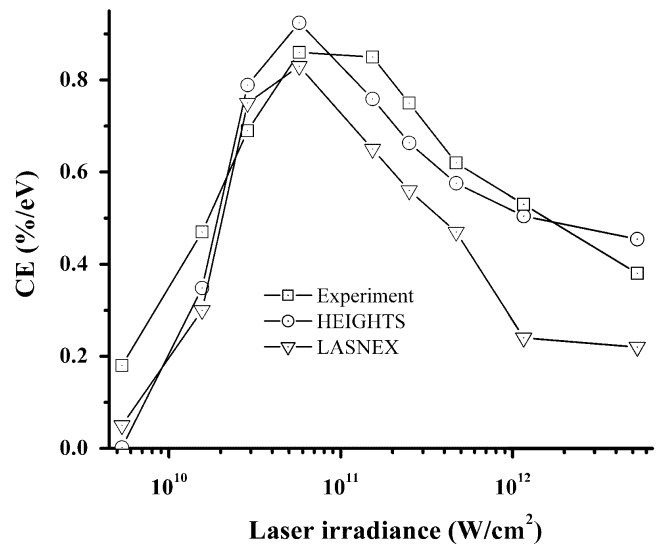
$$CE = \frac{Q_{EUV}^{13.4\,\text{nm}\pm1.1\,\text{eV}}}{Q_{las}\cdot 2.2\,\text{eV}}\cdot 100\%, \tag{27}$$

where $Q_{EUV}^{13.4\,\text{nm}\pm1.1\,\text{eV}}$ is the amount of EUV radiation energy that was registered in the 2.2 eV bandwidth centered at 13.4 nm, and Q_{las} is the total laser pulse energy. The efficiency is normalized to 1 eV. Opacities and atomic data that were used for the radiation transport and EUV calculations are reported in detail in Hassanein *et al.* (2003, 2004*a*, 2004*b*) and Morozov *et al.* (2004*a*, 2004*b*). Figure 3 presents a comparison of our HEIGHTS simulation results with experimental data (Spitzer, 1996) and theoretical modeling (calculated by the LASNEX code (Spitzer *et al.*, 1996; Zimmerman & Kruer, 1975)). As shown, HEIGHTS numerical results agree well with the published data. The numerical scheme used demonstrates the stability of our results even when spatial discretization is changed. Some deviation of our results from the published data can be explained due to certain arbitrariness of the initial data. The laser pulse shape and the laser irradiation distribution of the experiment at the laser spot are unknown. This important data would lead to a correction of the results. The HEIGHTS results in Figure 3 are calculated for laser pulsed power that is square in time. The irradiation spatial distribution by laser spot was assumed to be Gaussian.

3. PROBLEM DESCRIPTION

We focused our numerical modeling on a tin target material because of its current interest as a source for 13.5 nm EUV lithography (Aota & Tomie, 2005; Richardson *et al.*, 2004*a*; Choi *et al.*, 2000). Many investigators have optimized the tin target geometry, the laser pulse and prepulse characteristics, and the device chamber design in order to increase the

EUV source efficiency, mitigate the debris, and to improve the overall device performance. An ideal version of the EUV lithography light source is to have a small spherical target with high enough density and with optimum temperature (of given source material) for maximum EUV emission. This approach is used in recent investigations (Krücken *et al.*, 2004; Richardson *et al.*, 2004*b*) for the study of the EUV efficiency enhancement, that is, the first part of the CE problem: capability of target material of efficient EUV radiation at the 13.5 nm range of the background emission spectrums (White *et al.*, 2005). The second part of the problem consists in the formation and efficient confinement of the EUV plasma in optimal conditions (temperature plus enough density). Typical axial distributions of the temperature, density, and EUV flux are plotted in Figure 4 for the case of a tin target and single laser beam. As shown, the EUV output region is a thin layer between area with high temperature and low density, and area with high density but low temperature. The enlarging of this region will enable us to solve the second part of the EUV CE problem. Different target materials have their own EUV region size, which appears in different sizes of EUV source images (Stamm, 2004*a*).

Our preliminary calculations showed that a very thin EUV layer for the lithium target in comparison to the tin target. Laser radiation is actively absorbed by the target surface plasma and overheats the surface because lithium has only three electrons. The greater part of the laser energy occurs in this overheated area. The remaining part is distributed in the full target because at ~ 1 eV, lithium is transparent for the 1.064-μm laser radiation. Moreover, the hot external plasma layer absorbs intense EUV radiation from the thin EUV region in the lithium target case. As a result, these negative factors can appreciably decrease the attractiveness of certain element as candidates for the laser target. These factors can be avoided in two ways: (1) use more complex targets where the material combines clusters and (2) increase the preheated plasma density. The first way is
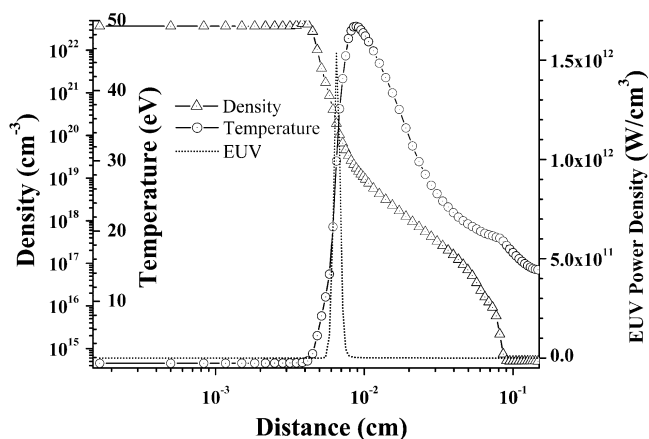
being actively investigated (Kubiak *et al.*, 1999). We consider the second way in the presented numerical simulations. Miyamoto *et al.* (2005) observed an increase in the EUV emission near the wall located close to the laser target. In our opinion, this effect is concerned with confinement of motion of the heated plasma. The density of the hot plasma increases near the wall and a new EUV region appears in this area. Thus, the experiment is not applicable to the full CE problem in real devices: additional wall creates additional shield for EUV output and decreases the final conversion efficiency. A better way is to produce an EUV transparent wall that can confine the heated plasma. We found an example of such a transparent wall in the experimental works of de Bruijn *et al.* (2003, 2005), where the prepulse initiates a shock wave in Xe gas plasma and the main laser pulse uses the initiated shock wave for the plasma confinement. The plasma confinement efficiency of such device (de Bruijn *et al.*, 2003, 2005) is not high, but it increases EUV output.

We propose to use a "self-confined" laser beam pulse to increase the EUV output. Modern development of the laser has made it possible to use hollow laser beams (Eardley, 2006; Padgett & Allen, 2000; Courtial *et al.*, 1997; Heckenberg *et al.*, 1992; Schaumann *et al.*, 2005; Kruglov *et al.*, 1992). To accelerate the plasma jet confinement and to test our hypothesis, we designed a LPP device with a laser beam that has a special distribution of the spot irradiation. As we assumed, the proposed device avoids the disadvantages noted above. Figure 5 schematically represents this LPP device with a planar tin target and with a hollow laser beam as an energy source. We assumed the initiation, confinement, and power supply of the cumulative plasma jet inside
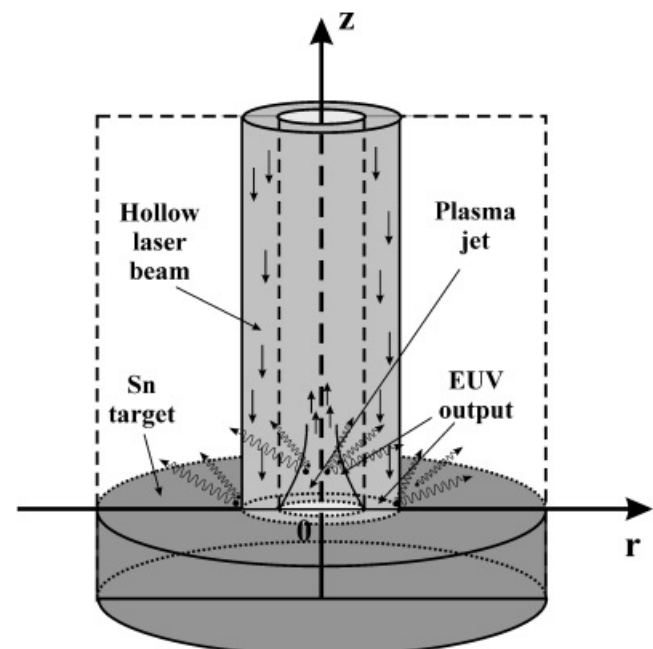

Fig. 4. Distributions of plasma density, temperature, and EUV power along laser beam axis at 9.0 ns time moment.

Fig. 5. Schematic illustration of the proposed hollow-beam LPP device.

the hollow laser beam by such device. The dense plasma jet should be initiated at the target surface inside the laser beam and should be confined with more heated plasma of the cylindrical laser volume.

4. SIMULATION RESULTS

We calculated the CE of our proposed new device as a function of the hole and beam ratio ξ, namely, the ratio of laser hole radius to the external radius of the laser beam. $\xi = 0$ corresponds to a laser beam without a hole, and $\xi = 1$ corresponds to the limit case of a thin, infinitesimal laser beam. To recognize the plasma jet effect, we used the same laser pulse energy (300 mJ), laser pulse duration (7.5 ns), and radiation power density in the round laser spot (5.73×10^{10} W/cm^2) for all calculations, that is, for the full range of the ξ ratio. Also, we assumed square distributions of laser pulse energy in time and in space to avoid the influence of the irradiation field curvature.

The results confirmed our assumption about the generation and the confinement of the dense plasma jet inside the hollow laser beam. Moreover, we observed pinching of the plasma on the laser beam axis for a certain ξ ratio (~ 0.7). Figure 6 presents the density, temperature, and velocity distributions of the hollow laser produced plasma in the *r-z* plane for $\xi = 0.7$ at time 7.0 ns. Figure 6c indicates the cumulative character of the initiated dense plasma jet because the plasma velocity inside the laser beam is much more than the velocity of the surrounding plasma. This effect can be used outside the EUV lithography applications for accelerating the laser plasma for different purposes.

The conversion efficiency of the hollow beam device was calculated from Eq. (27). We carried out numerical simulations for conditions close to those described in Section 2.3 (calculated EUV output in the 2.2-eV bandwidth centered at 13.4 nm). The radiation energy distribution in the Section 2.3 laser beam was Gaussian in space. The Gaussian space distribution is closer to actual experimental laser beam parameters and gives a higher CE in comparison to the simple square distribution. For this reason, the data for the planar target Figure 3 cannot be compared directly with the hollow beam device. However, the results do suggest that the hollow beam cumulative jet gives an abrupt increase of the EUV-output conversion efficiency. Figure 7 shows an increase of the CE by 17% for the case of time and space nonoptimized square distribution. We expect an increase of the final EUV efficiency of the hollow-beam LPP device after optimizing the initial parameters such as laser power density distribution in time and space, laser pulse duration, target geometry, and target structure.

5. CONCLUSION

We have presented an integrated model, HEIGHTS, to describe the hydrodynamics and optical processes that occur in LPP devices. HEIGHTS package combines the MHD theory of
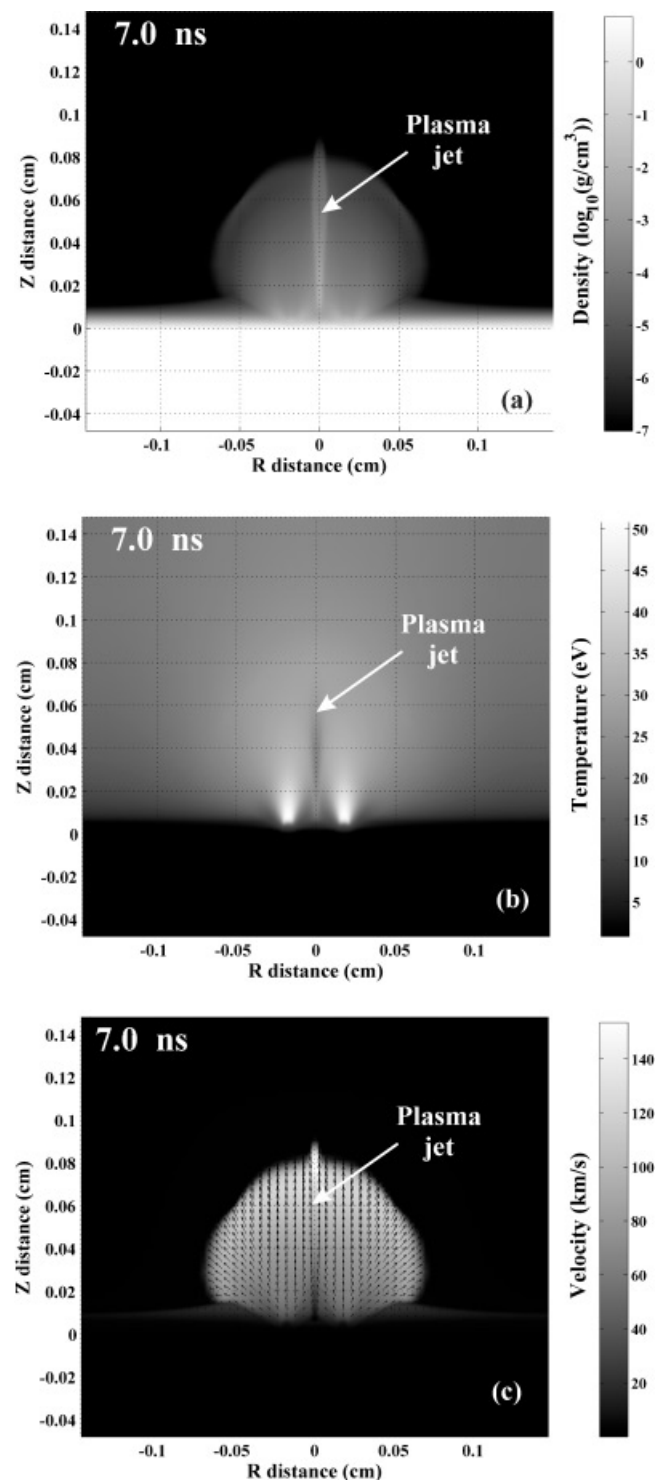

Fig. 6. Density (**a**), temperature (**b**), and velocity (**c**) of tin plasma distributions at 7.0 ns in *z-r* plane for hollow laser beam (laser energy, 300 mJ; wavelength, 1064 nm; $\xi = 0.7$).

plasma motion, models of magnetic diffusion and thermal conduction in plasma, radiation transport model, and laser absorption model. These theoretical models were adopted for numerical solution in the one- and two-temperature
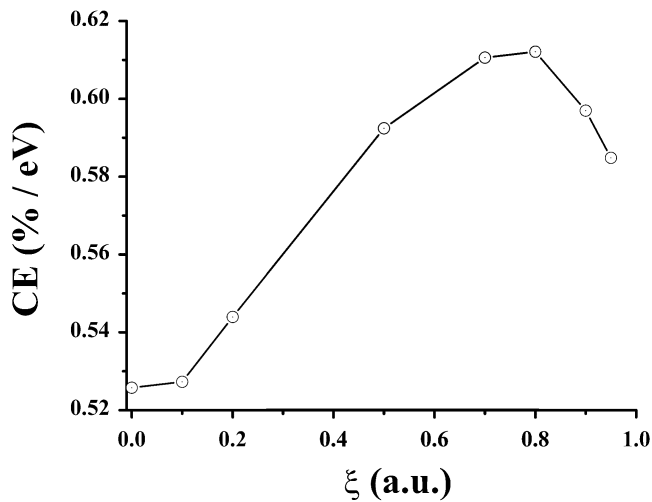
Fig. 7. Efficiency of the hollow-beam LPP device as a function of the radius ratio ($\xi = r_{hole}/r_{beam}$) for planar Sn target.

approximation. A simulation algorithm based on the separation of the physical processes was developed. For each physical process, the most efficient numerical scheme was used. Hydrodynamic processes were simulated on the basic of the total variation-diminishing scheme in the Lax–Friedrich formulation, and an implicit scheme based on the sparse matrix solver was developed for magnetic diffusion and heat conduction problems. Monte Carlo methods were used for simulating radiation transport and laser absorption processes.

The HEIGHTS package was tested and benchmarked against known analytical and experimental data. The results presented in this paper are calculated with two-dimensional version of the developed package, which was optimized for calculating the EUV output of LPP devices for lithography purposes. The theoretical models and computer simulation allowed investigating the influence of complex spatial effects of plasma motion on the final CE of the LPP device.

The effect of the cumulative plasma jet formation inside a hollow laser beam was predicted by computer simulation. The dense plasma jet increases the device conversion efficiency by about 17% compared for a planar tin target. The obtained spatial effects can be used to increase the efficiency of industrial LPP sources for EUV lithography. Further investigations of the jet influence on the final CE of LPP devices will involve the optimization of initial parameters such laser power density distribution in time and space, laser pulse duration, target geometry, and target structure.

ACKNOWLEDGMENTS

REFERENCES

AOTA, T. & TOMIE, T. (2005). Ultimate efficiency of extreme ultraviolet radiation from a laser-produced plasma. *Phys. Rev. Lett.* **94**, 015004.

ATTWOOD, D. (2004). Extreme ultraviolet light sources for semiconductor manufacturing. *J. Phys. D* **37**(23).

BAKSHI, V. (2006). EUV source technology: challenges and status. In *EUV Sources for Lithography* (Bakshi, V., Ed.), Ch. 1, pp. 3–25. Bellingham, WA: SPIE.

BRAGINSKII, S.I. (1965). Transport processes in a plasma. In *Reviews of Plasma Physics* (Leontovich, M.A., Ed.), Vol. 1, p. 205. New York: NY: Consultants Bureau.

CHOI, I.W., DAIDO, H., YAMAGAMI, S., NAGAI, K., NORIMATSU, T., TAKABE, H., SUZUKI, M., NAKAYAMA, T. & MATSUI, T. (2000). Detailed space-resolved characterization of a laser-plasma soft-x-ray source at 13.5-nm wavelength with tin and its oxides. *J. Opt. Soc. Am. B* **17**, 1616–1625.

COLOMBANT, D.G. & WINSOR, N.K. (1977). Thermal-force terms and self-generated magnetic fields in laser-produced plasmas. *Phys. Rev. Lett.* **38**, 697–701.

COURTIAL, J., DHOLAKIA, K., ALLEN, L. & PADGETT, M.J. (1997). Second-harmonic generation and the conservation of orbital angular momentum with high-order laguerre-gaussian modes. *Phys. Rev. A* **56**, 4193–4196.

DATTOLI, G., OTTAVIANI, P.L. & RENIERI, A. (2005). Free electron laser high gain devices. *Laser Part. Beams* **23**, 303–307.

DE BRUIJN, R., KOSHELEV, K. & BIJKERK, F. (2003). Enhancement of laser plasma EUV emission by shockwave–plasma interaction. *J. Phys. D* **36**, L88.

DE BRUIJN, R., KOSHELEV, K.N., ZAKHAROV, S.V., NOVIKOV, V.G. & BIJKERK, F. (2005). Enhancement of laser plasma extreme ultraviolet emission by shockwave–plasma interaction. *Phys. Plasma* **12**, 042701.

DESAI, T. & PANT, H.C. (2000). Control of Rayleigh–Taylor instabilities in laser accelerated seeded targets. *Laser Part. Beams* **18**, 119–128.

DUNN, J., FILEVICH, J., SMITH, R.F., MOON, S.J., ROCCA, J.J., KEENAN, R., NILSEN, J., SHLYAPTSEV, V.N., HUNTER, J.R., NG, A. & MARCONI, M.C. (2005). Picosecond 14.7 nm interferometry of high intensity laser-produced plasmas. *Laser Part. Beams* **23**, 9–13.

EARDLEY, M. (2006). Hollow laser beams. http://grad.physics.sunysb.edu/~meardley/hollow.

FAENOV, A., PIKUZ, T., MAGUNOV, A., BATANI, D., LUCCHINI, G., CANOVA, F. & PISELLI, M. (2004). Bright, point X-ray source based on a commercial portable 40 ps Nd:YAG laser system. *Laser Part. Beams* **22**, 373–379.

FIEDOROWICZ, H. (2005). Generation of soft X-rays and extreme ultraviolet (EUV) using a laser-irradiated gas puff target. *Laser Part. Beams* **23**, 365–373.

GOLDMAN, S.R. & SCHMALZ, R.F. (1987). Magnetic field behavior beyond the laser spot. *Phys. Fluids* **30**, 3608–3615.

HARILAL, S.S., O'SHAY, B. & TILLACK, M.S. (2005). Debris mitigation in a laser-produced tin plume using a magnetic field. *J. Appl. Phys.* **98**, 036102.

HASSANEIN, A., SIZYUK, V., TOLKACH, V., MOROZOV, V. & RICE, B.J. (2003). HEIGHTS initial simulation of discharge-produced plasma hydrodynamics and radiation transport for EUV lithography. *Proc. SPIE* **5037**, 714–727.

HASSANEIN, A., SIZYUK, V., TOLKACH, V., MOROZOV, V. & RICE, B.J. (2004*a*). HEIGHTS initial simulation of discharge produced plasma hydrodynamics and radiation transport for extreme ultraviolet lithography. *J. Microlith. Microfab. Microsyst.* **3**, 130–138.

HASSANEIN, A., SIZYUK, V., TOLKACH, V., MOROZOV, V., SIZYUK, T., RICE, B.J. & BAKSHI, V. (2004*b*). Simulation and optimization of DPP hydrodynamics and radiation transport for EUV lithography devices. *Proc. SPIE* **5374**, 413–422.

HECKENBERG, N.R., MCDUFF, R., SMITH, C.P. & WHITE, A.G. (1992). Generation of optical phase singularities by computer-generated holograms. *Opt. Lett.* **17**, 221–223.

JOHNSTON, T.W. & DAWSON, J.M. (1973). Correct values for high-frequency power absorption by inverse bremsstrahlung in plasmas. *Phys. Fluids* **16**, 722.

KEYSER, C., SCHRIEVER, G., RICHARDSON, M. & TURCU, E. (2003). Studies of high-repetition-rate laser plasma EUV sources from droplet targets. *Appl. Phys. A* **77**, 217–221.

KOVENYA, V.M., LEBEDEV, A.S. & CHERNY, S.G. (1988). Numerical algorithms for solving the Euler and Navier-Stokes equations on the basis of the splitting up method. In *Computational Fluid Dynamics* (Davis, G.S. & Fletcher, C., Eds.), pp. 303–315. Amsterdam: North-Holland.

KRÜCKEN, T., BERGMANN, K., JUSCHKIN, L. & LEBERT, R. (2004). Fundamentals and limits for the EUV emission of pinch plasma sources for EUV lithography. *J. Phys. D* **37**, 3213–3224.

KRUGLOV, V.I., LOGVIN, YU.A. & VOLKOV, V.M. (1992). The theory of spiral laser beams in nonlinear media. *J. Modern Opt.* **39**, 2277–2291.

KUBIAK, G.D., BERNARDEZ II, L.J., KRENZ, K.D. & SWEATT, W.C. (1999). Scale-up of a cluster jet laser plasma source for extreme ultraviolet lithography. *Proc. SPIE* **3676**, 669–678.

LABATE, L., GALIMBERTI, M., GIULIETTI, A., GIULIETTI, D., GIZZI, L.A., KOSTER, P., LAVILLE, S. & TOMASSINI, P. (2004). Ray-tracing simulations of a bent crystal X-ray optics for imaging using laser-plasma X-ray sources. *Laser Part. Beams* **22**, 253–259.

LEVEQUE, R.J. (2002). *Finite volume methods for hyperbolic problems*. Cambridge, UK: Cambridge University Press.

LEVINSON, H.J. (2001). *Principles of Lithography*. Bellingham, WA: SPIE.

MILOSHEVSKY, G.V., SIZYUK, V.A., PARTENSKII, M.B., HASSANEIN A. & JORDAN, P.C. (2006). Application of finite-difference methods to membrane-mediated protein interactions and to heat and magnetic field diffusion in plasmas. *J. Comp. Phys.* **212**, 25–51.

MIYAMOTO, S., AMANO, S., INOUE, T., SHIMOURA, A., KAKU, K., NICA, P.-E., KINUGASA, H. & MOCHIZUKI, T. (2005). EUV source developments on laser-produced plasmas using Xe cryogenic target and Li new scheme target. http://www.sematech.org/meetings/archives.htm.

MOORE, G.E. (1965). Cramming more components onto integrated circuits. *Electronics* **38**, 114.

MORA, P. (1981). Magnetic field generation in the underdense plasma. *Phys. Fluids* **24**, 2219–2226.

MOROZOV, V., SIZYUK, V., HASSANEIN, A. & TOLKACH, V. (2004*a*). Simulation of discharge produced plasma and EUV radiation in various z-pinch devices. Report No. ANL-ET-04/31. Argonne, IL: Argonne National Laboratory.

MOROZOV, V., TOLKACH, V. & HASSANEIN, A. (2004*b*). Calculation of tin atomic data and plasma properties. Report ANL-ET-04/24. Argonne, IL: Argonne National Laboratory.

MYERS, D.W., FOMENKOV, I.V., HANSSON, B.A.M., KLENE, B.C. & BRANDT, D.C. (2005). EUV source system development update: Advancing along the path to HVM. *Proc. SPIE* **5751**, 248–259.

NAKAMURA, T., SAKAGAMI, H., JOHZAKI, T., NAGATOMO, H. & MIMA, K. (2006). Generation and transport of fast electrons inside cone targets irradiated by intense laser pulses. *Laser Part. Beams* **24**, 5–8.

OZAKI, T., KIEFFER, J.-C., TOTH, R., FOURMAUX, S. & BANDULET, H. (2006). Experimental prospects at the Canadian advanced laser light source facility. *Laser Part. Beams* **24**, 101–106.

PADGETT, M. & ALLEN, L. (2000). Light with a twist in its tail. *Contemp. Phys.* **41**, 275–285.

PANKERT, J., APETZ, R., BERGMANN, K., DERRA, G., JANSSEN, M., JONKERS, J., KLEIN, J., KRUECKEN, T., LIST, A., LOEKEN, M., METZMACHER, C., NEFF, W., PROBST, S., PRUMMER, R., ROSIER, O., SEIWERT, S., SIEMONS, G., VAUDREVANGE, D., WAGEMANN, D., WEBER, A., ZINK, P. & ZITZEN O. (2005). Integrating Philips' extreme UV source in the alpha-tools. *Proc. SPIE* **5751**, 260–271.

RICHARDSON, M., KOAY, C.-S., TAKENOSHITA, K., KEYSER, C. & AL-RABBAN, M. (2004*a*). High conversion efficiency mass-limited Sn-based laser plasma source for extreme ultraviolet lithography. *J. Vac. Sci. Technol. B* **22**, 785–790.

RICHARDSON, M., KOAY, C.-S., TAKENOSHITA, K., KEYSER, C., GEORGE, S., TEERAWATTANSOOK, S., AL-RABBAN, M. & SCOTT, H. (2004*b*). Laser plasma EUVL sources: progress and challenges. *Proc. SPIE* **5374**, 447–453.

SCHAUMANN, G., SCHOLLMEIER, M.S., RODRIGUEZ-PRIETO, G., BLAZEVIC, A., BRAMBRINK, E., GEISSEL, M., KOROSTIY, S., PIRZADEH, P., ROTH, M., ROSMEJ, F.B., FAENOV, A.YA., PIKUZ, T.A., TSIGUTKIN, K., MARON, Y., TAHIR, N.A. & HOFFMANN, D.H.H. (2005). High energy heavy ion jets emerging from laser plasma generated by long pulse laser beams from the NHELIX laser system at GSI. *Laser Part. Beams* **23**, 503–512.

SIEGEL, R. & HOWELL, J. (1981). *Thermal Radiation Heat Transfer*. Bellingham, WA: Hemisphere.

SILVERMAN, P.J. (2002). The Intel Lithography Roadmap. *Intel Tech. J.* **3**, 55–61.

SIZYUK, V. & HASSANEIN, A. (2002). Hydrodynamic phenomena of gas-filled chamber due to target implosion in IFE systems. Report No. ANL-ET-02/26, Argonne, IL: Argonne National Laboratory.

SIZYUK, V., HASSANEIN, A., MOROZOV, V., TOLKACH, V., SIZYUK T. & RICE, B. (2006). Numerical simulation of laser-produced plasma devices for EUV lithography using the heights integrated model. *Num. Heat Transf. A* **49**, 215–236.

SPITZER, L. (1962). *Physics of Fully Ionized Gases*, 2nd Ed. New York, NY: Interscience.

SPITZER, R.C., ORZECHOWSKI, T.J., PHILLION, D.W., KAUFFMAN, R.L. & CERJAN, C.J. (1996). Conversion efficiencies from laser-produced plasmas in the extreme ultraviolet regime. *J. Appl. Phys.* **79**, 2251–2258.

STAMM, U. (2004*a*). EUV source development at XTREME technologies—an update. http://www.sematech.org/meetings/archives/litho/euvl/20041101euvl/presentations/day1/So02_U_Stamm.pdf

STAMM, U. (2004*b*). Extreme ultraviolet light sources for use in semiconductor lithography—state of the art and future development. *J. Phys. D* **37**, 3244–3253.

THAREJA, R.K. & SHARMA, A.K. (2006). Reactive pulsed laser ablation: Plasma studies. *Laser Part. Beams* **24**, 311–320.

TÓTH, G. & ODSTRČIL, D. (1996). Comparison of some flux corrected transport and total variation diminishing numerical schemes for hydrodynamic and magnetohydrodynamic problems. *J. Comp. Phys.* **128**, 82–100.

TÓTH, G. (2000). The $\nabla \cdot B = 0$ constraint in shock-capturing magnetohydrodynamics codes. *J. Comp. Phys.* **161**, 605–652.

ULLRICH, A., KORNER, H.J., KROTZ, W., RIBITZKI, G., MURNICK, D.E., MATTHIAS, E., KIENLE, P. & HOFFMANN, D.H.H. (1987). Heavy-ion excitation of rare-gas excimers. *J. Appl. Phys.* **62**, 357–361.

WAGNER, T., EBERL, E., FRANK, K., HARTMANN, W., HOFFMANN, D.H.H. & TKOTZ, R. (1996). XUV amplification in a recombining z-pinch plasma. *Phys. Rev. Lett.* **76**, 3124–3127.

WHITE, J., HAYDEN, P., DUNNE, P., CUMMINGS, A., MURPHY, N., SHERIDAN, P. & O'SULLIVAN, G. (2005). Simplified modeling of 13.5 nm unresolved transition array emission of a Sn plasma and comparison with experiment. *J. Appl. Phys.* **98**, 113301.

WIDNER, M.M. (1973). Self-generated magnetic fields in laser plasmas. *Phys. Fluids* **16**, 1778–1780.

ZELDOVICH, YA. & RAIZER, YU. (1966). *Physics of Shock Waves and High-Temperature Hydrodynamics Phenomena*. New York, NY: Academic.

ZIMMERMAN, G.B. & KRUER, W.L. (1975). Numerical simulation of laser-initiated fusion. *Comments Plasma Phys. Contr. Fusion* **2**, 51–61.